# Novel Optical Biosensor Based on a Nano-Gold Coated by Schiff Base Doped in Sol/Gel Matrix for Sensitive Screening of Oncomarker CA-125

M.N. Abou-Omar, M.S. Attia, H.G. Afify, M.A. Amin, Rabah Boukherroub, E.H. Mohamed

ACS OMEGA

http://pubs.acs.org/journal/acsodf

Article

# Novel Optical Biosensor Based on a Nano-Gold Coated by Schiff Base Doped in Sol/Gel Matrix for Sensitive Screening of Oncomarker CA-125

Mona N. Abou-Omar, Mohamed S. Attia,* Hisham G. Afify, Mohammed A. Amin, Rabah Boukherroub, and Ekram H. Mohamed

Cite This: *ACS Omega* 2021, 6, 20812−20821

Read Online

ACCESS | Metrics & More | Article Recommendations | Supporting Information

**ABSTRACT:** The urge for sensitive, facile, minimally invasive, and fast detection method of CA-125, a significant and crucial biomarker in ovarian malignancy, is currently substantial. This paper describes the detailed construction and characterization of a newly designed optical nano-biosensor to detect CA-125 accurately and sensitively. The fabricated sensor consists of a nano-gold thin film doped into a matrix of sol−gel, exhibiting a centered fluorescence band at 423 nm when excited at 340 nm. The quantification of CA-125 relies on its quenching ability of this fluorescence signal. The sensor was challenged to evaluate its sensitivity and specificity in detecting CA-125 present in samples collected from ovarian cancer diagnosed patients and compared to samples from healthy women as a control. Our findings revealed that the developed biosensor had a sensitivity of 97.35% and a specificity of 94.29%. Additionally, a wide linearity range over 2.0−127.0 U mL$^{-1}$ for CA-125 was achieved with a detection limit of 1.45 U mL$^{-1}$. Furthermore, the sensor could successfully discriminate samples between healthy and diseased people, which demonstrates its suitability in CA-125 assessment.

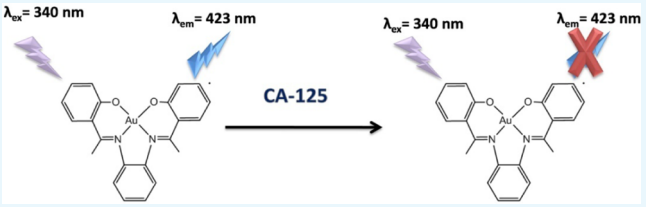


## 1. INTRODUCTION

Among all women's gynecological cancers, ovarian cancer (OC) and particularly the epithelial subtype is ranked as the second most frequently diagnosed one. It is featured with an average 5-year survival rate of around 50%, whereas around 75% of the cases are usually diagnosed at advanced stages, i.e., third and fourth.[1] Because of the nonspecific symptoms and omnipresent clinical manifestations, including abdominal discomfort, pelvic pain, and indefinite vaginal bleeding, the OC is usually underdiagnosed especially in early stages after the occurrence of metastasis, leading to bad prognosis and high mortality rate.[2]

Extensive efforts were exerted by scientists and gynecologists worldwide for the sake of the early diagnosis of OC and implementing different effective screening strategies to improve the survival rates.[3,4] Up to date, cancer antigen (CA-125), also termed mucin 16 or carbohydrate antigen, has been considered to be the most popular tumor marker and the gold standard in OC in all aspects, since its discovery in 1981.[5−7]

The CA-125 normal cutoff range is 0−35 U mL$^{-1}$, and nearly 90% of women suffering from epithelial OC (EOC) exhibit raised serum levels. Unfortunately, CA-125 level could also be elevated in various physiological conditions such as pregnancy and menstruation, in addition to pathological conditions including benign cases and non-OCs.[4]

Despite the low specificity, the utility of CA-125 as a diagnostic biomarker in OC diagnosis is still significant where it could be recruited using advanced trends. Among these trends, one approach adopted statistical and arithmetic algorithms as significant tools for the diagnosis and discrimination between malignant and benign ovarian tumors as the risk of malignancy index, risk of malignancy algorithm, multivariate index assay, and the risk of OC algorithm, known as RMI, ROCA, OVA1, and ROMA,[3] respectively.[8] Another approach used a multi-biomarker panel in which the CA-125 level was measured in combination with at least two other biomarkers. This strategy improved the sensitivity of diagnosis and allowed to decrease the probability of false results.[9−11]

The differentiation between OC and endometriosis, which is difficult to be realized without a surgery, could also be achieved via screening the CA-125 level in combination with other inflammatory and hematological markers such as D-dimer and the neutrophil-to-lymphocyte ratio.[6]

**Received:** April 13, 2021
**Accepted:** June 15, 2021
**Published:** August 3, 2021

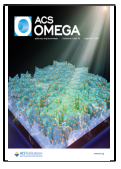

Table 1. Different Nanoparticle-Based Sensors for Bioanalysis of Cancer Antigen (CA-125)

| no. | nanoparticle-based sensors | linearity range | limit of detection |
|---|---|---|---|
| | Electrochemical/Electrochemiluminescence Technique | | |
| 1 | polyamidoamine−gold nanoparticles with multiwall carbon nanotubes (CNTs) and a reduced graphene oxide-based immunosensor[23] | 0.0005−75 U $mL^{-1}$ | 6 $\mu$U $mL^{-1}$ |
| 2 | conductive nanoink composed of silver nanoparticles deposited on graphene quantum dots functionalized with D-penicillamine on a glassy carbon electrode[24] | 0.001−400 U $mL^{-1}$ | 0.001 U $mL^{-1}$ |
| 3 | gold nanostructure−gallium nitride-based aptasensor[25] | 1−100 U $mL^{-1}$ | 0.3 U $mL^{-1}$ |
| 4 | conductive silver nanoink-based biosensor[26] | 0.01−400 U $mL^{-1}$ | 0.01 U $mL^{-1}$ |
| 5 | gold nanoparticles in a microfluidic biosensor[27] | 84 000, 35 000, and 3500 U $mL^{-1}$ | |
| 6 | gold and platinum nanostructure-modified carbon screen-printed electrode[28] | 450−2.9 $\mu$g $mL^{-1}$ | 419 ± 31 ng $mL^{-1}$ for the Au interface; 386 ± 27 ng $mL^{-1}$ for the Pt interface |
| 7 | silver nanoparticle-doped amidoxime-modified polyacrylonitrile nanofiber-based aptasensor[29] | 0.01−350 U $mL^{-1}$ | 0.0042 U $mL^{-1}$ |
| 8 | molecular imprinted polymer on gold electrode[30] | 0.01−500 U $mL^{-1}$ | 0.01 U $mL^{-1}$ |
| 9 | chitosan−gold nanoparticle and CNT-based immunosensor[31] | 0.01−0.5 and 0.5−100 U $mL^{-1}$ | 0.002 U $mL^{-1}$ |
| 10 | dual gold nanoparticle-based immunosensor[32] | 20−100 U $mL^{-1}$ | 3.4 U $mL^{-1}$ |
| 11 | carboxylated multiwalled CNTs deposited on reduced graphene oxide film-based aptasensor[33] | 1.0 × $10^{-9}$−1.0 U $mL^{-1}$ | 5.0 × $10^{-10}$ U $mL^{-1}$ |
| 12 | nanocomposite of polyamidoamine dendrimer CdTe@CdS quantum dots conjugated with polyamidoamine sulfanilic acid $Ru(bpy)_3^{2+}$-based biosensor[34] | 1 $\mu$U $mL^{-1}$ to 1 U $mL^{-1}$ | 0.1 $\mu$U $mL^{-1}$ |
| 13 | a network of DNA aptamer and CNT platform on a chip[35] | $10^{-12}$−$10^{-6}$ g $mL^{-1}$ | 10 pg $mL^{-1}$ |
| 14 | multiwalled CNT-embedded zinc oxide nanofiber-based biosensor[36] | 0.001 U $mL^{-1}$ to 1 kU $mL^{-1}$ | 0.00113 U $mL^{-1}$ |
| 15 | zinc oxide nanorod−gold nanoparticle nanohybrid-based immunosensor[37] | 2.5 ng $\mu L^{-1}$ to 1 $\mu$g $L^{-1}$ | 2.5 ng $\mu L^{-1}$ |
| 16 | hierarchical gold nanostructure-modified bioelectrode[38] | 10−100 U $mL^{-1}$ | 5.5 U $mL^{-1}$ |
| 17 | silica-coated gold nanoparticles on a modified gold electrode[39] | 0−0.1 U $mL^{-1}$ | 0.0016 U $mL^{-1}$ |
| 18 | core−shell gold−silver nanoparticle-based immunosensor[40] | 1.0−150 IU $mL^{-1}$ | 1.0 IU $mL^{-1}$ |
| | Fluorescence Technique | | |
| 19 | phthalocyanine-doped polystyrene nanocomposite biosensor[41] | 1.0 × $10^{-2}$−127 U $mL^{-1}$ | 1.0 × $10^{-4}$ U $mL^{-1}$ |
| 20 | $Fe_3O_4$@gold magnetic bead-based aptasensor[42] | 0.5−30.0 ng $mL^{-1}$ | 0.15 pg $mL^{-1}$ |
| 21 | DNA-functionalized silver−gold and silver nanoclusters in combination with graphene oxide-based aptasensor[43] | 1.33−200 ng $mL^{-1}$ | 0.18 ng $mL^{-1}$ |
| 22 | two blue/green luminescent carbon dots and 2D $MoS_2$-based biosensor[44] | 0.05−8 pg $mL^{-1}$ | 5.0 fg $mL^{-1}$ |
| 23 | carbon dots functionalized with aptamer in combination with a dendrimer/gold nanoparticle-based immunosensor[45] | 2.5 × $10^3$−2 × $10^4$ cells/mL | 400 cells/$mL^{-1}$ |
| 24 | graphene quantum dot-based biosensor[46] | 0.1−600 U $mL^{-1}$ | 0.05 U $mL^{-1}$ |

CA-125 has also a significant utility as a prognostic indicator and considered to be a standard component in the overall management of EOC.[12] After debulking surgery, the sequential or serial measurement of CA-125 in the serum of OC patients, besides studying its kinetics, half-life, nadir, and normalization, has a great impact on monitoring therapeutic outputs, treatment response, malignancy recurrence, tumor burden, and survival outcomes.[13,14]

It could be comprehended that therapeutic decisions, undertaken throughout the whole treatment course starting from diagnosis to monitoring the disease regression in response to the medical intervention and ending up with patient follow-up, are postulated principally in accordance with laboratory findings of CA-125. Thus, continuous investigations are frequently conducted with the aim to develop new reliable methods for accurate assaying CA-125 in different biological fluids.[15]

The standard quantification method relies on the antibody recognition of the epitope region of CA125, adopting the enzyme-linked immune sorbent assay principle.[16] The restrictions of this technique, exemplified by reagent autoantibodies and high-dose hook effect along with reported inharmonious results, call for more reliable quantification methods.[17] Therefore, several techniques were proposed, such as Raman spectroscopy,[18] mass spectrometry,[19,20] and electrochemical impedance spectroscopy.[21] Even though these methods allowed to achieve enhanced sensitivity and specificity, their wide clinical application is hindered by their need of sophisticated expensive instruments, tedious sample preparation, qualified personnel for operation, and incompatibility with high throughput demand.

Recently, the tremendous development in nanoscience[22] enabled the successful application of nanotechnology in biosensing of CA-125 with high sensitivity and more efficiently,[23−46] as summarized in Table 1.

Among the developed platforms, luminescence-based sensors are very attractive, owing to their efficiency, ease of operation, rapid response time, and enhanced sensitivity. Metal nanostructures displaying localized surface plasmon resonance such as gold nanoparticles are suitable in this field. Obviously, there are numerous studies that utilized gold nanoparticles in CA-125 detection.[27,31,40] Even though these sensing platforms achieved enhanced sensitivity, they all relied on the coupling of the CA-125 antibody to the nanoparticles' surface. In this way, the limitations of immunosensing are not fully resolved. Different from the developed approaches described in the literature, the present study reports on a very selective, sensitive, low-cost, and less-time consuming method for CA-125 quantification, by exploiting the quenching ability of gold nanoparticles shielded by a Schiff base ligand embedded in a thin sol−gel film.

Upon the protection of gold nanoparticles by a monolayer of Schiff base ligands, peculiar features were displayed, including molecule-like HOMO−LUMO energy gaps and single-



https://doi.org/10.1021/acsomega.1c01974
ACS Omega 2021, 6, 20812−20821

electron charging, allowing its employment in chemical and optical sensing.[47,48]

## 2. EXPERIMENTAL SECTION

**2.1. Instrumentation.** See Section S1 for more details.

**2.2. Chemicals and Patient Samples.** See Section S2 for more details.

**2.3. Methodology.** *2.3.1. Preparation of 2,2′-((1E,1′E)-(1,2-Phenylenebisazanylylidene) Bis(ethane-1-yl-ylidene)-diphenol Schiff Base.* This Schiff base was prepared following Chiririwa and Muzenda's report,[49] as briefly illustrated in Scheme 1. See Section S3 for more details.

**Scheme 1. Schiff Base and Gold−Schiff Base Complex Preparation**

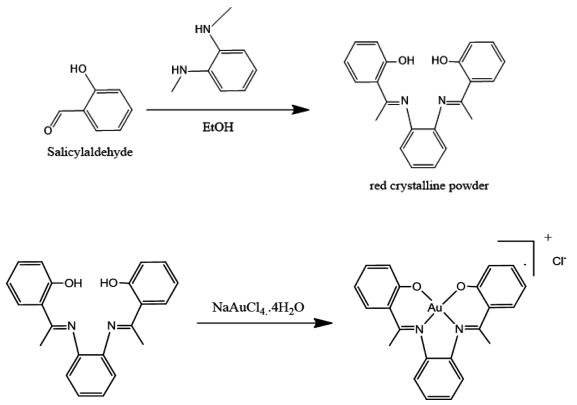


*2.3.2. Gold (III)−Schiff Base Complex Preparation.* The complex of gold−Schiff base was obtained through adding Schiff base solution dissolved in 10.0 mL of dry dichloromethane to an equimolar amount of [$NaAuCl_4 \cdot 4H_2O$] dissolved in 10.0 mL of dry ethanol. The obtained mixture was stirred overnight in a bath of ice, followed by the solvent reduction to 5.0 mL and product precipitation utilizing hexane. To afford crystalline complex, hot methanol was used to dissolve the crude solid, and benzene was used for recrystallization. The obtained crystalline complex was finally washed with diethyl ether and vacuum dried (Scheme 1).

*2.3.3. Gold−Schiff Base Complex-Doped Sol−Gel Nano-Optical Sensor Preparation.* Before the preparation step, distilled water containing polyethylene glycol (PEG) as a surfactant was used for cleaning the substrate. Ultrasonication was then performed for 30 min in a water:PEG mixture and another 10 min in acetone, followed by boiling in 2-propanol for another 10 min. Finally, the substrate was rinsed with 2-propanol, spun dried, and spin coated.

The preparation of the biosensor was performed following nearly the same procedures previously reported for the fabrication of a uric acid sensor[50] with the introduction of some modifications to minimize sensor crack. In short, 8.0 mL of the prepared $5.0 \times 10^{-4}$ mol $L^{-1}$ Au (III) Schiff base complex in ethanol was mixed with 2.0 mL of tetraethyl orthosilicate (TEOS), 2.0 mL of diethoxydimethylsilane, and 2.0 mL of deionized water. The prepared solution (9.0 mL) was used for filling glass vials with a diameter of 24.0 mm and a height of 48.0 mm, and para-film was used for stoppering the filled vials where three small holes were made after 2 days. Six days later, the preparation of thin films from the solution that was partially hydrolyzed and condensed was achieved via spin coating (2000 rpm for 30 s). The process was performed on quartz small slides with a width of 8.5 mm and a height of 25.0 mm to be capable of fitting in a cuvette for fluorescence intensity measurement.

The developed nano-biosensor was thoroughly characterized using Fourier transform infrared (FTIR) spectroscopy, UV−vis, transmission electron microscopy (TEM), X-ray diffraction (XRD), and atomic force microscopy techniques. The thickness of the thin film is 0.12 mm, as determined by a micrometer.

*2.3.4. Serum Preparation.* Serum was isolated from the collected blood samples, following a standard serum isolation protocol. For the removal of all proteins, citrate solution (3.0 mL) was mixed with plasma (4.0 mL), followed by centrifugation (4000 rpm for 150 min) and decantation. To prepare the test solution (TS), the obtained serum (1.0 mL) was mixed with phosphate buffer (0.1 mL) and added to the thin film, previously fabricated, in the cuvette where water (1.9 mL) was added.

*2.3.5. Proposed Method.* In the cell containing previously prepared TS, an aliquot equivalent to 100 $\mu$L of various CA-125 standard concentrations, in water, was added to the gold−Schiff base complex thin film doped in the sol−gel matrix. Recording of the fluorescence spectra was achieved at $\lambda_{ex}/\lambda_{em}$ = 340/423 nm. After each estimation, rinsing of the optical sensor with water was performed. The construction of a calibration graph was done through plotting the measured $(F_0/F) - 1$ at $\lambda_{em}$ = 423 nm versus the respective CA-125 concentration.

The presented method's selectivity and validity were investigated through testing the effect of different possible interfering species on the intensity of fluorescence after the addition of 130.0 U $mL^{-1}$ of CA-125, and the tolerable limit was calculated. The studied interfering species included 130.0 U $mL^{-1}$ of each of CEA (CA 15-3 and CA 19-9), $2.0 \times 10^{-3}$ mol $L^{-1}$ of both NaCl and KCl, 0.08 g $L^{-1}$ of both uric acid and glucose, 0.06 g $L^{-1}$ of both urea and triglycerides, 0.7 g $L^{-1}$ of albumin, and 0.01 g $L^{-1}$ of total protein.

The biosensor performance was assessed for the following parameters:

1. Sensitivity could be defined as the screening test capability for true positive detection, reflecting its ability to identify all diseased people correctly.[51,52]
2. Specificity could be described as the screening test capability for true negative detection and the identification of people who do not suffer the disease correctly.[51,52]
3. Positive predictive value (PPV) could be defined as the probability that people displaying positive screening test results actually have the disease under investigation.
4. Negative predictive value (NPV) could be defined as the probability that people displaying negative screening test results actually do not suffer the disease under investigation.
5. Disease prevalence could be calculated simply using the following equation: $T_{disease}$/total × 100.

## 3. RESULTS AND DISCUSSION

**3.1. Characterization of the Thin Film.** The sol−gel thin film doped with Au nanoparticles coated by the Schiff base ligand with a thickness of 0.12 mm was characterized using various tools. The TEM image in Figure 1 revealed a dense


https://doi.org/10.1021/acsomega.1c01974
ACS Omega 2021, 6, 20812−20821

thin film comprising spherical nanoparticles with a diameter of 19.4 ± 0.7 nm. See Section S4 for more details.

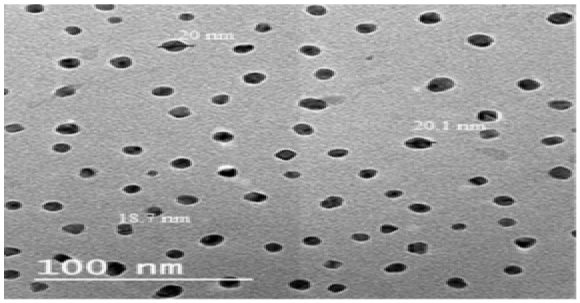


**Figure 1.** TEM image of the fabricated thin film containing Au nanoparticles coated by the Schiff base ligand doped in a sol–gel matrix.

FTIR spectroscopy was used to assess the chemical composition of the thin sol–gel film containing Au nanoparticles coated by the Schiff base ligand. The FTIR spectrum showed two bands: one band centered at 1014 $cm^{-1}$ assigned to the $(Si—O—Si)_n$ vibration mode and another band at 892 $cm^{-1}$ assigned to the Si—OH vibration mode confirming TEOS hydrolysis and condensation forming polymeric silica. Other bands observed at 3031, 2918, and 2842 $cm^{-1}$ correspond to the C—H, O—H symmetric, antisymmetric, and stretching modes.[53−55] Bands displayed at 1034 and 839 $cm^{-1}$ are assigned to the C—H in-plane rock and out-of-plane, respectively. The frequencies at 756 and 699 $cm^{-1}$ are ascribed the C—H out-of-plane modes of rings. The appearance of vibrational modes with energy less than 700 $cm^{-1}$ and bands at 533 and 453 $cm^{-1}$ is most probably the M—O bonds (M = Au, Si), ensuring the combination between the metallic ions and oxygen atoms in the silica gel network and Au—N bond,[53−55] respectively (Figure 2). The bands at 1603, 1489, and 1445 $cm^{-1}$ are C═N stretching frequencies, a key feature of Schiff base. It is noticeable from FTIR spectrum that the OH band of water is absent, which can be justified by the fabrication mechanism in which the formation of Si—O—Si bond took place between the matrix and the substrate.

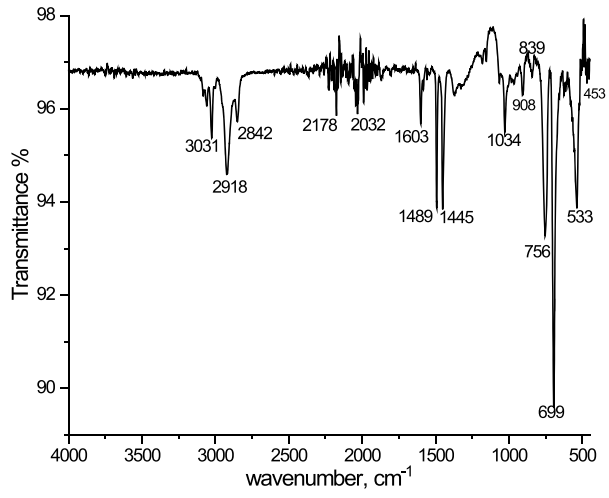


**Figure 2.** Thin sol–gel film containing Au nanoparticles coated by Schiff base ligand FTIR spectrum.

The XRD pattern of the thin film containing gold nanoparticles coated by Schiff base is displayed in Figure 3.

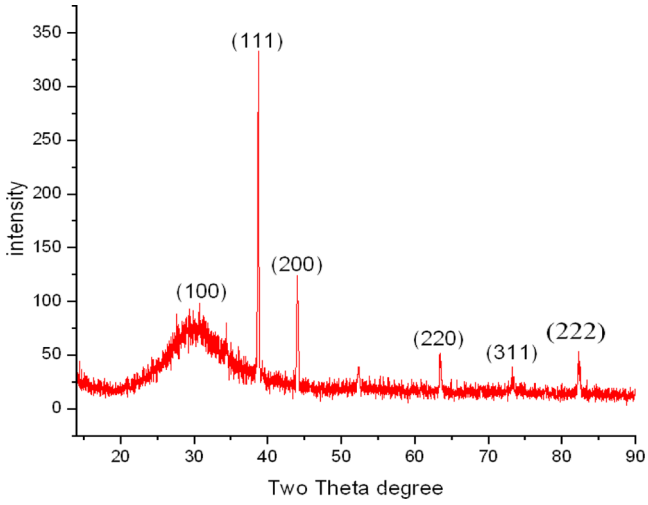


**Figure 3.** XRD pattern of the thin sol–gel film containing Au nanoparticles coated by Schiff base ligand.

The crystalline nature of gold nanoparticles was confirmed by the presence of obvious peaks of cubic phases (JCPDS no. 03-0921) at 38.2° (111), 44.3° (200), 64.9° (220), 77.5° (311), and 81.5° (222). The size of the gold nanoparticles was also suggested to be small, owing to the peaks' bottom broad width. The diffraction pattern comprised Bragg's reflections of gold, as indicated by the presence of five intense peaks ascribed to gold nanoparticles.[54] In addition, a diffraction peak due to the $SiO_2$ matrix was observed at $2\theta$ = 28° (100).

**3.2. Absorption and Emission Spectra.** The sol–gel film doped with the Au nanoparticles coated by Schiff base optical features assessed using UV–vis spectrophotometry. Figure 4 depicts the UV–vis absorption spectra in the absence and presence of CA-125. A clear absorption peak with high intensity was observed at 274 nm because of the $\pi \rightarrow \pi^*$ transition in the organic moiety of the Schiff base. The appearance of another broad peak at 548 nm was assigned to the gold nanoparticles' free electron surface plasmon

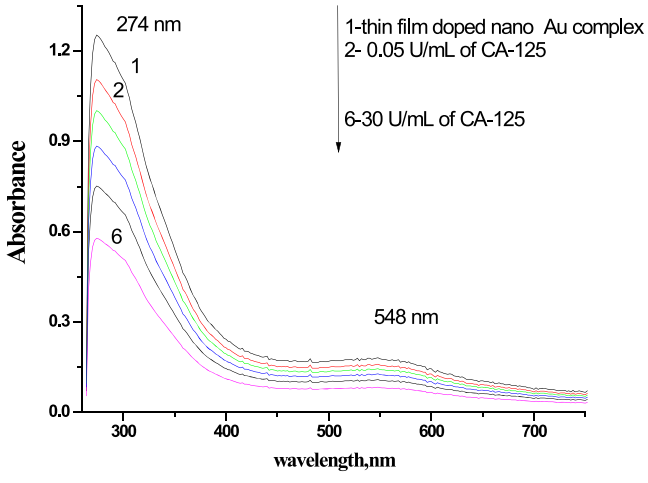


**Figure 4.** Sol–gel thin film containing Au nanoparticles coated by Schiff base ligand absorption spectra upon the addition of different concentrations of CA-125 protein.



https://doi.org/10.1021/acsomega.1c01974
ACS Omega 2021, 6, 20812−20821

oscillation.[56] The intensity of these peaks decreased substantially upon the addition of CA-125 protein, as presented in Figure 4, indicating that UV−vis spectrophotometry could potentially be applied for CA-125 sensing.

The fluorescence spectra ($\lambda_{ex}$ = 340 nm) of the thin sol−gel film containing AuNPs coated by Schiff base before and after the addition of different CA-125 concentrations are displayed in Figure 5. The lifetime of the AuNPs coated by Schiff base is

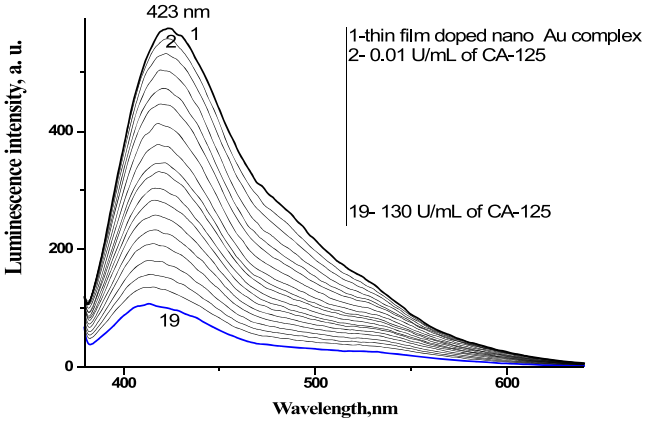


**Figure 5.** Thin sol−gel film containing AuNPs coated by Schiff base ligand fluorescence emission spectra at $\lambda_{ex}$ 340 nm after adding different CA-125 protein concentrations.

calculated to be 67 $\mu$s, and the quantum yield of its emission intensity equals $\Phi_{Au}$ = 0.188 by using quinine sulfate $\Phi_{ref}$ = 0.544 as a reference. The fluorescence intensity of the AuNPs coated by the Schiff base ligand at 423 nm was quenched by the addition of CA-125 protein in different concentrations (Figure 5). CA-125 as ligand attacks Au metal ion in Au−Schiff base complex from below and above of axial positions through its N-terminal domain (polar glycosylated tail), in which a sugar molecule is attached to an oxygen atom in an amino acid residue in a protein, the molecular geometry of Au is changed from square planar shape to distorted square planar shape. Quenching effect is ascribed to the prevention of free electron recombination from the conduction (sp) band to valence (d) band holes, where the electrons are preferentially transferred from the gold nanoparticles to CA-125 in the excited state, as illustrated in Figure 6.

**3.3. Analytical Parameters.** The effect of different solvents on the fluorescence intensity of the thin sol−gel film containing AuNPs coated by the Schiff base ligand was investigated, after establishing the same conditions and procedures adopted in the proposed method. Protic solvents (ethanol and water) contributed to the enhancement of the fluorescence intensity, as revealed by the results, because of their capability of stabilizing the sensor excited state. In contrast, aprotic solvents (acetonitrile, DMF, and DMSO) cause destabilization of the optical sensor excited sate, leading to the fluorescence intensity quenching. Moreover, a 24 nm blue-shift was observed because of the energy gap between the sp and d bands increased in the aprotic solvents.[57−64]

The results of the validity and selectivity assessment are presented in Figure 7. All tested interfering biomolecules

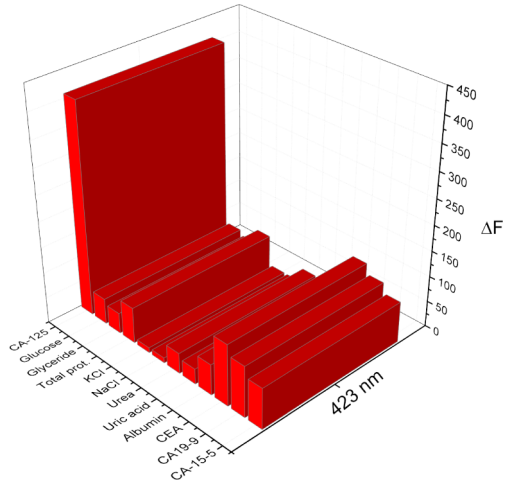


**Figure 7.** Interfering species influence on the optical sensor fluorescence intensity.

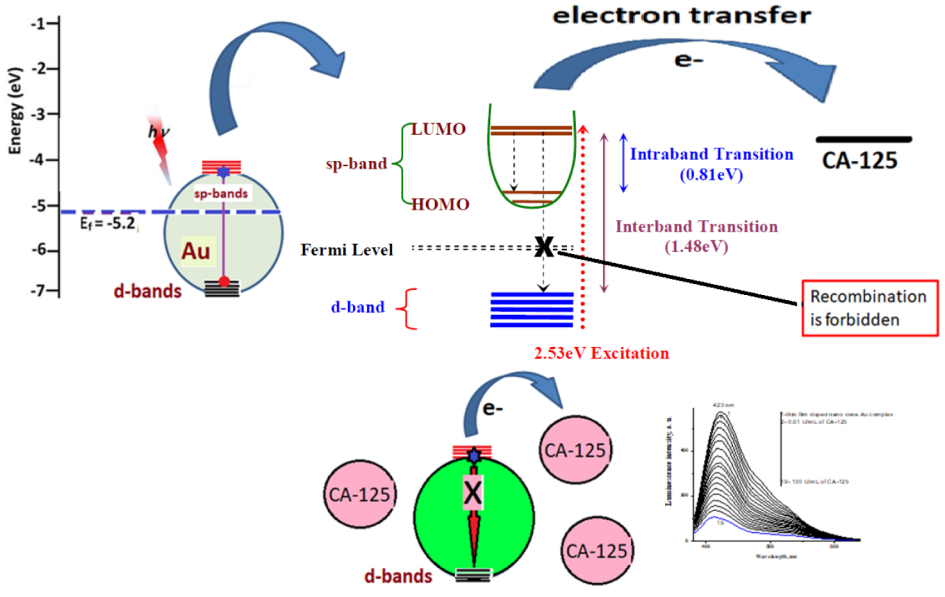


**Figure 6.** Mechanism of the quenching of the gold nanoparticles coated by a Schiff base ligand optical sensor by CA-125.



https://doi.org/10.1021/acsomega.1c01974
ACS Omega 2021, 6, 20812−20821

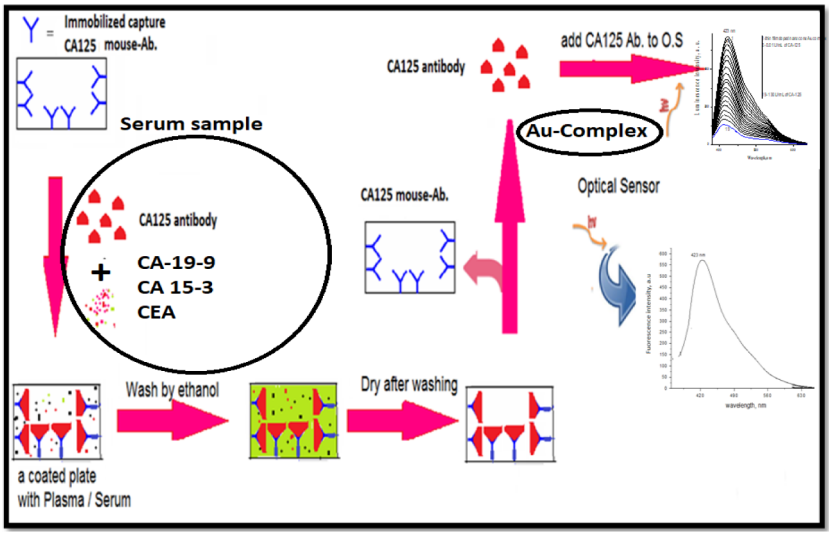


**Figure 8.** Proposed procedure to increase CA-125 nano-optical sensor selectivity.

exerted a minor effect on the fluorescence intensity. However, the copresence of CEA, CA 15-3, and CA 19-9 with CA-125 in the OC patients' serum sample induced a remarkable interference in CA-125 determination.

For tackling this interference, a preliminary sample preparation step is proposed in Figure 8,[41] in which serum samples were first incubated with CA-125 antibody. Later, antigen−antibody decoupling was performed and CA-125 concentration was measured using the developed optical nano-biosensor.

**3.4. Validation.** *3.4.1. Dynamic Linear Range.* The CA-125 concentration effect on the thin sol−gel film containing Au NPs coated by the Schiff base ligand optical sensor fluorescence intensity is depicted in Figure 9. The Stern−

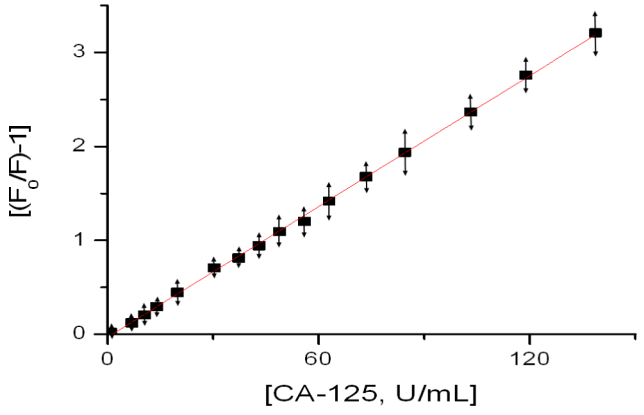


**Figure 9.** Calibration graph of the $(F_0/F) - 1$ against different concentrations of CA-125.

Völmer equation was employed to study the correlation between the CA-125 concentration and the optical sensor fluorescence intensity[65−67] (Section S5):

$$\frac{F_0}{F} - 1 = K_{sv}[Q]$$

where $F_0$ corresponds to the optical sensor fluorescence intensity in the absence of CA-125, $F$ is the optical sensor fluorescence intensity in the presence of CA-125, $Q$ is the CA-125 concentration, and $K_{sv}$ = 0.023 U mL$^{-1}$ represents the Stern−Völmer constant. Upon plotting $(F_0/F) - 1$ against CA-125 concentration, it is observed that as the CA-125 concentration increases, the fluorescence intensity increases in a linear relationship with a correlation coefficient $(r)$ = 0.999 over the CA-125 concentration range within 2.0−127 U mL$^{-1}$. The limit of detection (LOD) and limit of quantification (LOQ) were calculated in accordance with the guidelines of ICH,[68] and their values are tabulated in Table 2.

**Table 2. Sensitivity and Regression Parameters for the Developed Sensor**

| parameter | value |
|---|---|
| $\lambda_{em}$ (nm) | 423 |
| linear range (U mL$^{-1}$) | 2.0−128 |
| LOD (U mL$^{-1}$) | 1.45 |
| LOQ (U mL$^{-1}$) | 4.36 |
| regression equation, $Y^a$ | $Y = a + bX$ |
| intercept $(a)$ | 0.001 |
| slope $(b)$ | 0.021 |
| standard deviation | 0.01 |
| variance (Sa2) × 10$^{-4}$ | 1.0 |
| regression coefficient $(r)$ | 0.999 |

$^aY$ = fluorescence intensity; $X$ = concentration in nmol L$^{-1}$; $a$ = intercept; $b$ = slope.

*3.4.2. Accuracy.* The evaluation of the method accuracy was performed where the results were presented in the form of relative error (RE) between the CA-125 measured mean concentrations and the actual taken concentrations. The bias % was also determined at every single concentration, and the obtained results demonstrated the method accuracy (Table 3).

*3.4.3. Precision.* For the assessment of intraday precision (repeatability) and interday, 10 serum samples were analyzed in triplicates applying the general procedures previously detailed on the same day and within three successive days, respectively. The results were processed and values of %RSD assured the precision of the presented methods, and the results are summarized in Table 3.

*3.4.4. Application.* The proposed optical sensor analytical employability was investigated via measuring CA-125 concentration in five different serum samples of both healthy and 10


https://doi.org/10.1021/acsomega.1c01974
ACS Omega 2021, 6, 20812−20821

**Table 3. Evaluation of Intraday and Interday Accuracy and Precision of the Proposed Method in Case of Different Serum Samples**

| | standard method[3] | proposed method | | | | | | | | | | | | | | | |
|---|---|---|---|---|---|---|---|---|---|---|---|---|---|---|---|---|---|
| | | | | | | | | | | intraday precision | | | | interday precision | | | |
| serum sample | average ± RSD% | readings | | | average | RSD% | recovery% | *t*-test | *F*-test | average reading | CL | RE%[a] | RSD% | average reading | CL | RE% | RSD% |
| 1 | 12.1 ± 1.97 | 12.2 | 12.7 | 11.5 | 12.1 | 2.07 | 100.83 | 0.08 | 0.89 | 12.2 | 0.63 | 0.83 | 2.07 | 12.4 | 0.66 | 2.5 | 2.17 |
| 2 | 26.0 ± 1.72 | 25.5 | 26.7 | 27.2 | 26.4 | 1.42 | 101.53 | 0.46 | 1.42 | 26.7 | 0.95 | 1.53 | 1.42 | 26.8 | 1.02 | 3.07 | 1.52 |
| 3 | 29.1 ± 1.51 | 29.6 | 28.5 | 30.6 | 29.5 | 1.61 | 101.72 | 0.59 | 0.85 | 29.8 | 1.20 | 1.72 | 1.61 | 30.4 | 1.05 | 3.17 | 1.41 |
| 4 | 19.0 ± 1.42 | 17.6 | 18.9 | 19.0 | 18.5 | 1.92 | 97.36 | 1.25 | 0.57 | 18.9 | 0.90 | 2.63 | 1.92 | 19.4 | 0.93 | 2.63 | 1.98 |
| 5 | 18.0 ± 2.1 | 19.0 | 20.0 | 18.0 | 19.0 | 3.6 | 105.55 | 1.63 | 0.30 | 19.3 | 1.74 | 5.55 | 3.60 | 19.6 | 1.69 | 6.66 | 3.5 |
| 6 | 77.0 ± 1.23 | 76.9 | 77.9 | 77.6 | 77.4 | 1.39 | 100.51 | 0.07 | 0.77 | 77.6 | 2.73 | 0.51 | 1.39 | 80.6 | 2.93 | 4.41 | 1.49 |
| 7 | 98.0 ± 1.87 | 97.8 | 98.6 | 96.0 | 97.4 | 1.83 | 99.38 | 0.05 | 1.05 | 97.8 | 4.53 | 0.61 | 1.83 | 99.6 | 4.93 | 1.42 | 1.99 |
| 8 | 120 ± 0.89 | 122.7 | 121.0 | 121.6 | 121.7 | 1.02 | 101.41 | 1.07 | 0.74 | 121.9 | 3.15 | 1.41 | 1.02 | 124.2 | 4.08 | 3.33 | 1.32 |
| 9 | 84.0 ± 1.43 | 83.8 | 84.5 | 82.8 | 83.7 | 1.5 | 99.64 | 0.02 | 0.91 | 83.6 | 3.19 | 0.35 | 1.50 | 85.4 | 2.76 | 1.90 | 1.3 |
| 10 | 109.0 ± 0.88 | 108.8 | 110.6 | 109.6 | 109.6 | 1.01 | 100.55 | 0.16 | 0.75 | 109.8 | 2.81 | 0.55 | 1.01 | 112.2 | 5.60 | 2.75 | 2.01 |
| 11 | 113.0 ± 1.97 | 112.0 | 114.0 | 115.0 | 113.7 | 2.1 | 100.61 | 0.04 | 0.86 | 113.5 | 6.07 | 0.61 | 2.10 | 116.2 | 6.36 | 2.65 | 2.2 |
| 12 | 104.0 ± 2.71 | 106.0 | 107.0 | 103.0 | 104.7 | 2.98 | 100.67 | 0.02 | 0.81 | 104.9 | 7.94 | 0.67 | 2.98 | 106.2 | 8.26 | 1.90 | 3.1 |
| 13 | 198.0 ± 2.49 | 200.0 | 196.0 | 201.0 | 199.0 | 2.65 | 100.50 | 0.02 | 0.87 | 199.4 | 13.42 | 0.50 | 2.65 | 201.2 | 14.94 | 1.51 | 2.95 |
| 14 | 189.0 ± 2.87 | 192.0 | 187.0 | 191.0 | 190.0 | 3.1 | 100.52 | 0.02 | 0.84 | 190.6 | 14.99 | 0.52 | 3.10 | 192.2 | 13.10 | 1.58 | 2.71 |
| 15 | 230.0 ± 1.91 | 231.0 | 234.0 | 237.0 | 234.0 | 2.1 | 101.73 | 0.36 | 0.79 | 234.2 | 12.50 | 1.73 | 2.10 | 237.2 | 11.31 | 3.04 | 1.9 |

[a]RE: percent relative error, %RSD: relative standard deviation, and CL: confidence limits were calculated from: CL = $\pm tS/\sqrt{n}$. (the tabulated value of $t$ is 4.303 at the 95% confidence level; $S$ = standard deviation, and $n$ = number of measurements). Theoretical values of $t$- and $F$-tests at 95% confidence limits are 4.303 and 19.0, respectively.



https://doi.org/10.1021/acsomega.1c01974
ACS Omega 2021, 6, 20812−20821

women suffering OC within the 30−65 years age range. A good correlation between the average values recorded by the newly developed procedure and those obtained by the standard one was achieved (Table 3). In addition, the performance parameters of the optical sensor, previously discussed, were calculated, and the obtained results were as following: sensitivity = 97.35%, specificity = 94.29, PPV = 89.45%, NPV = 91.75%, and prevalence of disease = 71.51%.

## 4. STATISTICAL ANALYSIS

The *t* and *F* tests were performed, and the results were obtained at 95% confidence level, indicating that there were no significant differences between the standard[69] and newly developed methods, as presented in Table 3.

## 5. CONCLUSIONS

In the present study, a novel nano-optical sensor, consisting of a thin sol−gel film containing gold nanoparticles coated by Schiff base ligand, was proposed and successfully applied for CA-125 determination in serum samples of healthy and women suffering OC. The technique developed in this work could be considered as an excellent contribution to the analytical methods used for CA-125 determination. The method owns several features such as rapidity, accuracy, and sensitivity.

## ■ ASSOCIATED CONTENT

### Supporting Information

The Supporting Information is available free of charge at https://pubs.acs.org/doi/10.1021/acsomega.1c01974.

Instrumentation S1; chemicals and patient samples S2; preparation of 2,2′-((1*E*,1′*E*)-(1,2-phenylenebisazanylylidene) bis(ethane-1-yl-ylidene)diphenol Schiff base S3; characterization of the thin film S4; and the dynamic linear range and Stern−Völmer equation S5 (PDF)

## ■ AUTHOR INFORMATION


### Corresponding Author

**Mohamed S. Attia** − *Chemistry Department, Faculty of Science, Ain Shams University, Cairo 11566, Egypt;* orcid.org/0000-0001-6074-7366; Phone: +202-1229867311; Email: mohd_mostafa@sci.asu.edu.eg

### Authors

**Mona N. Abou-Omar** − *Department of Chemistry, Faculty of Women for Arts, Science and Education, Ain Shams University, Cairo 13013, Egypt*

**Hisham G. Afify** − *Department of Chemistry, Faculty of Women for Arts, Science and Education, Ain Shams University, Cairo 13013, Egypt*

**Mohammed A. Amin** − *Department of Chemistry, College of Science, Taif University, Taif 21944, Saudi Arabia;* orcid.org/0000-0001-7024-8034

**Rabah Boukherroub** − *Univ. Lille, CNRS, Centrale Lille, Univ. Polytechnique Hauts-de-France, UMR 8520 − IEMN, F-59000 Lille, France*

**Ekram H. Mohamed** − *Pharmaceutical Chemistry Department, Faculty of Pharmacy, The British University in Egypt, 11837 El Sherouk City, Cairo, Egypt*

Complete contact information is available at: https://pubs.acs.org/10.1021/acsomega.1c01974


### Notes

The authors declare no competing financial interest.

## ■ ACKNOWLEDGMENTS

The authors would like to express sincere thanks to researchers in Taif University (Taif, Saudi Arabia), who offered full support to the project no. TURSP-2020/03.

## ■ REFERENCES


(1) Torre, L. A.; Trabert, B.; DeSantis, C. E.; Miller, K. D.; Samimi, G.; Runowicz, C. D.; Gaudet, M. M.; Jemal, A.; Siegel, R. L. Ovarian cancer statistics. *Ca-Cancer J. Clin.* **2018**, *68*, 284−296.

(2) Sun, Y.; Xu, J.; Jia, X. The Diagnosis Treatment, Prognosis and Molecular Pathology of Borderline Ovarian Tumors: Current Status and Perspectives. *Cancer Manage. Res.* **2020**, *12*, 3651−3659.

(3) Das, P. M.; Bast, R. C. Early detection of ovarian cancer. *Biomark Med.* **2008**, *2*, 291−303.

(4) Gupta, V.; Bernardini, M. Q. Algorithms Used in Ovarian Cancer Detection: A Mini review on Current and Future Applications. *J. Appl. Lab. Med.* **2018**, *3*, 290−299.

(5) Scholler, N.; Urban, N. CA 125 in ovarian cancer. *Bio. Med.* **2007**, *1*, 513−523.

(6) Chen, J.; Huang, Q.; Wan, T.; Tu, H.; Gu, H.; Cao, J. The Challenges and Opportunities of LncRNAs in Ovarian Cancer Research and Clinical Use. *J. Ovarian. Res.* **2017**, *12*, 1−8.

(7) Nagtegaal, S. H.; Hulsbergen, A. F.; Van Dorst, E. B.; Kavouridis, V. K.; Jessurun, C. A.; Broekman, M. L.; Smith, T. R.; Verhoeff, J. J. Age, pathology and CA-125 are prognostic factors for survival in patients with brain metastases from gynaecological tumours. *Clin. Transl. Rad. Oncol.* **2020**, *24*, 11−15.

(8) Dochez, V.; Caillon, H.; Vaucel, E.; Dimet, J.; Winer, N.; Ducarme, G. Biomarkers and algorithms for diagnosis of ovarian cancer: CA125, HE4, RMI and ROMA, a review. *J. Ovarian Res.* **2019**, *12*, 1−9.

(9) Chen, F.; Shen, J.; Wang, J.; Cai, P.; Huang, Y. Clinical analysis of four serum tumor markers in 458 patients with ovarian tumors: Diagnostic value of the combined use of HE4, CA125, CA19-9, and CEA in ovarian tumors. *Cancer Manage. Res.* **2018**, *10*, 1313−1318.

(10) Muinao, T.; Deka Boruah, H. P.; Pal, M. Multi-biomarker panel signature as the key to diagnosis of ovarian cancer. *Heliyon* **2019**, *5*, No. e02826.

(11) Whitwell, H. J.; Worthington, J.; Blyuss, O.; Gentry-Maharaj, A.; Ryan, A.; Gunu, R.; Kalsi, J.; Menon, U.; Jacobs, I.; Zaikin, A.; Timms, J. F. Improved early detection of ovarian cancer using longitudinal multimarker models. *Mol. Diagn.* **2020**, *122*, 847−856.

(12) Gupta, D.; Lis, C. G. Role of CA125 in predicting ovarian cancer survival - a review of the epidemiological literature. *J. Ovarian Res.* **2009**, *2*, 1−20.

(13) Colakovic, S.; Lukiç, V.; Mitroviç, L.; Jeliç, S.; Susnjar, S.; Marinkoviç, J. Prognostic value of CA125 kinetics and half-life in advanced ovarian cancer. *Int. J. Biol. Markers* **2000**, *15*, 147−152.

(14) Zeng, J.; Huang, H.; Shan, Y.; Li, Y.; Jin, Y.; Pan, L. The effect of CA125 nadir level on survival of advanced-stage epithelial ovarian carcinoma after interval debulking surgery. *J. Cancer* **2017**, *8*, 3410−3415.

(15) Razmi, N.; Hasanzadeh, M. Current advancement on diagnosis of ovarian cancer using biosensing of CA 125 biomarker: Analytical approaches. *TrAC, Trends Anal. Chem.* **2018**, *108*, 1−12.

(16) Shojaeian, S.; Allameh, A.; Zarnani, A.; Chamankhah, M.; Ghods, R.; AliBayat, A. A.; Jeddi-Tehrani, M. Production and Characterization of Monoclonal Antibodies against the Extracellular Domain of CA 125. *Immunol. Invest.* **2010**, *39*, 114−131.

(17) Ward, G.; Simpson, A.; Boscato, L.; Hickman, P. The investigation of interferences in immunoassay. *Clin. Biochem.* **2017**, *50*, 1306−1311.

(18) Paraskevaidi, M.; Ashton, K. M.; Stringfellow, H. F.; Wood, N. J.; Keating, P. J.; Rowbottom, A. W.; Martin-Hirsch, P. L.; Martin, F.

L. Raman spectroscopic techniques to detect ovarian cancer biomarkers in blood plasma. *Talanta* **2018**, *189*, 281−288.
(19) Weiland, F.; Fritz, K.; Oehler, M. K.; Hoffmann, P. Deciphering the Molecular Nature of Ovarian Cancer Biomarker CA125. *Int. J. Mol. Sci.* **2012**, *13*, 9942−9958.
(20) Pan, Y.; Nikitin, A. M.; Araizi, G.; Huang, Y. K.; Matsushita, Y.; Naka, T.; de Visser, A. Rotational symmetry breaking in the topological superconductor SrxBi2Se3 probed by upper-critical field experiments. *Sci. Rep.* **2016**, *6*, No. 28632.
(21) Gazze, A.; Ademefun, R.; Gazze, A.; Ademefun, R.; Conlan, R. S.; Teixeira, S. R. Electrochemical impedence spectroscopy enabled CA125 detection; toward early ovarian cancer diagnosis using graphene biosensors. *J. Interdiscip. Nanomed.* **2016**, *3*, 82−88.
(22) Farzin, L.; Shamsipurb, M.; Samandarib, L.; Sadjadia, S.; Sheibania, S. HIV biosensors for early diagnosis of infection: The intertwine of nanotechnology with sensing strategies. *Talanta* **2020**, *206*, 1−14.
(23) Pakchin, P. S.; Fathi, M.; Ghanbari, H.; Saber, R.; Omidi, Y. A novel electrochemical immunosensor for ultrasensitive detection of CA125 in ovarian cancer. *Biosens. Bioelectron.* **2020**, *153*, No. 112029.
(24) Saadati, A.; Hassanpour, S.; Bahavarniadef, F.; Mohammad, H. M. A novel biosensor for the monitoring of ovarian cancer tumor protein CA 125 in untreated human plasma samples using a novel nano-ink: A new platform for efficient diagnosis of cancer using paper based microfluidic technology. *Anal. Methods* **2020**, *12*, 1639−1649.
(25) Hu, D.; Liang, H.; Wang, X. Highly Sensitive and Selective Photoelectrochemical Aptasensor for Cancer Biomarker CA125 Based on AuNPs/GaN Schottky Junction. *Anal. Chem.* **2020**, *92*, 10114−10120.
(26) Jafaria, M.; Hasanzadeh, M.; Solhi, E.; Soodabeh, H.; Shadjou, S.; Mokhtarzadeh, N.; Jouyban, A.; Mahboob, A. Biosensing of prostate specific antigen (PSA) in human plasma samples using biomacromolecule encapsulation into KCC-1-npr-NH2: A new platform for prostate cancer detection. *Int. J. Biol. Macromol.* **2019**, *126*, 1255−1265.
(27) Nunna, B. B.; Mandal, D.; Lee, J. U.; Singh, H.; Zhuang, S.; Misra, D.; Bhuyian, M. U.; Lee, E. S. Detection of cancer antigens (CA-125) using gold nano particles on interdigitated electrode-based microfluidic biosensor. *Nano Convergence* **2019**, *6*, 1−12.
(28) Baradoke, A.; Jose, B.; Pauliukaite, R.; Forster, R. J. Properties of Anti-CA125 antibody layers on screen-printed carbon electrodes modified by gold and platinum nanostructures. *Electrochim. Acta* **2019**, *306*, 299−306.
(29) Farzin, L.; Sadjadi, S.; Shamsipur, M.; Sheibani, S.; Mousazadeh, M. H. Employing AgNPs doped amidoxime-modified polyacrylonitrile (PAN-oxime) nanofibers for target induced strand displacement-based electrochemical aptasensing of CA125 in ovarian cancer patients. *Mater. Sci. Eng., C.* **2019**, *97*, 679−687.
(30) Rebelo, T. S.; Costa, R.; Brandão, A. T.; Silva, A. F.; Sales, M. G.; Pereira, C. M. Molecularly imprinted polymer SPE sensor for analysis of CA-125 on serum. *Anal. Chim. Acta* **2019**, *1082*, 126−135.
(31) Pakchin, P. S.; Ghanbari, H.; Saber, R.; Omidi, Y. Electrochemical immunosensor based on chitosan-gold nanoparticle/carbon nanotube as a platform and lactate oxidase as a label for detection of CA125 oncomarker. *Biosens. Bioelectron.* **2018**, *122*, 68−74.
(32) Kumar, N.; Sharma, S.; Nara, S. Dual gold nanostructure-based electrochemical immunosensor for CA125 detection. *Appl. Nanosci.* **2018**, *8*, 1843−1853.
(33) Majd, S. M.; Salimi, A. Ultrasensitive flexible FET-type aptasensor for CA 125 cancer marker detection based on carboxylated multiwalled carbon nanotubes immobilized onto reduced graphene oxide film. *Anal. Chimica Acta* **2018**, *1000*, 273−282.
(34) Babamiri, B.; Hallaj, R.; Salimi, A. Ultrasensitive electrochemiluminescence immunoassay for simultaneous determination of CA125 and CA15-3 tumor markers based on PAMAM-sulfanilic acid-Ru(bpy)32+ and PAMAM-CdTe@CdS nanocomposite. *Biosens. Bioelectron.* **2018**, *99*, 353−360.
(35) Gedi, V.; Song, C. K.; Kim, G. B.; Lee, J. O.; Oh, E.; Shin, B. S.; Jung, M.; Shim, J.; Lee, H.; Kim, Y. Sensitive on-chip detection of cancer antigen 125 using a DNA aptamer/carbon nanotube network platform. *Sens. Actuators, B* **2018**, *256*, 87−97.
(36) Paul, K. B.; Singh, V.; Vanjari, S. R.; Singh, S. G. One step biofunctionalized electrospun multiwalled carbon nanotubes embedded zinc oxide nanowire interface for highly sensitive detection of carcinoma antigen-125. *Biosens. Bioelectron.* **2017**, *88*, 144−152.
(37) Gasparotto, G.; Costa, J. P.; Costa, P. I.; Zaghete, M. A.; Mazon, T. Electrochemical immunosensor based on ZnO nanorods-Au nanoparticles nanohybrids for ovarian cancer antigen CA-125 detection. *Mater. Sci. Eng., C* **2017**, *76*, 1240−1247.
(38) Torati, S. R.; Kasturi, K. C.; Lim, B.; Kim, C. Hierarchical gold nanostructures modified electrode for electrochemical detection of cancer antigen CA125. *Sens. Actuators, B* **2017**, *243*, 64−71.
(39) Johari-Ahar, M.; Rashidi, M. R.; Barar, J.; Aghaie, M.; Mohammadnejad, D.; Ramazani, A.; Karami, P.; Coukosde, G.; Omidi, Y. An ultra-sensitive impedimetric immunosensor for detection of the serum oncomarker CA-125 in ovarian cancer patients. *Nanoscale* **2015**, *7*, 3768−3779.
(40) Raghav, R.; Srivastava, S. Core−shell gold−silver nanoparticles based impedimetric immunosensor for cancer antigen CA125. *Sens. Actuators, B* **2015**, *220*, 557−564.
(41) Attia, M. S.; Ali, K.; El-Kemary, M.; Darwish, W. M. Phthalocyanine-doped polystyrene fluorescent nanocomposite as a highly selective biosensor for quantitative determination of cancer antigen 125. *Talanta* **2019**, *201*, 185−193.
(42) Xie, L.; Cao, Y.; Hu, F.; Li, T.; Wang, Q.; Gan, N. Microfluidic chip electrophoresis for simultaneous fluorometric aptasensing of alpha-fetoprotein, carbohydrate antigen 125 and carcinoembryonic antigen by applying a catalytic hairpin assembly. *Microchim. Acta* **2019**, *186*, 1−10.
(43) Wang, Y.; Wang, S.; Lu, C.; Yang, X. Three kinds of DNA-directed nanoclusters cooperating with graphene oxide for assaying mucin 1, carcinoembryonic antigen and cancer antigen 125. *Sens. Actuators, B* **2018**, *262*, 9−16.
(44) Hamd-Ghadareh, S.; Salimi, A.; Parsa, S.; Fathi, F. Simultaneous biosensing of CA125 and CA15-3 tumor markers and imaging of OVCAR-3 and MCF-7 cells lines via bi-color FRET phenomenon using dual blue-green luminescent carbon dots with single excitation wavelength. *Int. J. Biol. Macromol.* **2018**, *118*, 617−628.
(45) Hamd-Ghadareh, S.; Salimi, A.; Fathi, F. B. An amplified comparative fluorescence resonance energy transfer immunosensing of CA125 tumor marker and ovarian cancer cells using green and economic carbon dots for bio-applications in labeling, imaging and sensing. *Biosens. Bioelectron.* **2017**, *96*, 308−316.
(46) Al-Ogaidi, I.; Gou, H.; Aguilar, Z. P.; Guo, S.; Melconian, A. K.; Al-Kazaz, A. K.; Meng, F.; Wu, N. Detection of the ovarian cancer biomarker CA-125 using chemiluminescence resonance energy transfer to graphene quantum dots. *Chem. Commun.* **2014**, *50*, 1344−1346.
(47) Nam, J. M.; Thaxton, C. S.; Mirkin, C. A. Nanoparticle-based bio-bar codes for the ultrasensitive detection of proteins. *Science* **2003**, *301*, 1884−1886.
(48) Schaaff, T. G.; Shafigullin, M. N.; Khoury, J. T.; Vezmar, I.; Wettern, R. L. Properties of a Ubiquitous 29 kDa Au:SR Cluster Compound. *J. Phys. Chem. B* **2001**, *105*, 8785−8796.
(49) Chiririwa, H.; Muzenda, E. Characterization of Gold (III) Complexes and an in vitro Evaluation of their Cytotoxic Properties. *J. Pharm. Sci.* **2014**, *2*, 637−640.
(50) Hashem, S. G.; Elsaady, M. M.; Afify, H. G.; Omer, W. E.; Youssef, A. O.; El-Kemary, M.; Attia, M. S. Determination of uric acid in serum using an optical sensor based on binuclear Pd(II) 2-pyrazinecarboxamide-bipyridine doped in a sol gel matrix. *Talanta* **2019**, *199*, 89−96.
(51) Attia, M. S.; AlRadadi, N. S. Progress of pancreatitis disease biomarker alpha amylase enzyme by new nano optical sensor. *Biosens. Bioelectron.* **2016**, *86*, 413−419.
(52) Attia, M. S.; AlRadadi, N. S. Nano optical sensor binuclear Pt-2-pyrazinecarboxylic acid -bipyridine for enhancement of the efficiency


https://doi.org/10.1021/acsomega.1c01974
*ACS Omega* 2021, 6, 20812−20821

of 3-nitrotyrosine biomarker for early diagnosis of liver cirrhosis with minimal hepatic encephalopathy. *Biosens. Bioelectron.* **2016**, *86*, 406−412.
(53) Efimov, A. M.; Pogareva, V. G. Water-related IR absorption spectra for some phosphate and silicate glasses. *J. Non-Cryst. Solids* **2000**, *275*, 189−198.
(54) Mie, G. Contributions to the optics of cloudy media, especially colloidal metal solutions. *Ann. Phys.* **1908**, *25*, 377−445.
(55) Rao, V. M.; Kumar, A. R.; Neeraja, K.; Veeraiah, N.; Reddy, M. R. Optical and structural investigation of Eu3+ ions in Nd3+ co-doped magnesium lead borosilicate glasses. *J. Alloys Compd.* **2013**, *557*, 209−217.
(56) Wang, H.; Huff, T. B.; Zweifel, D. A.; He, W.; Low, P. S.; Wei, A.; Cheng, J. X. In vitro and in vivo two-photon luminescence imaging of single gold nanorods. *Proc. Natl. Acad. Sci. U. S. A.* **2005**, *102*, 15752−15756.
(57) Hamed, E.; Attia, M. S.; Synthesis, B. K. Spectroscopic and Thermal Characterization of Copper(II) and Iron(III) Complexes of Folic Acid and Their Absorption Efficiency in the Blood. *Bioinorg. Chem. Appl.* **2009**, *2009*, No. 979680.
(58) Attia, M. S.; Mahmoud, W. H.; Youssef, A. O.; Mostafa, M. S. Cilostazol determination by the enhancement of the green emission of Tb3+ optical sensor. *J. Fluoresc.* **2011**, *21*, 2229−2235.
(59) Attia, M. S.; Ramsis, M. N.; Khalil, L. H.; Hashem, S. G. Spectrofluorimetric assessment of chlorzoxazone and Ibuprofen in pharmaceutical formulations by using Eu-tetracycline HCl optical sensor doped in sol−gel matrix. *J. Fluoresc.* **2012**, *22*, 779−788.
(60) Elabd, A.; Zidan, W.; Abdaly, M. M.; Bakir, E.; Attia, M. S. Uranyl ions adsorption by novel metal hydroxides loaded Amberlite IR120/sol-gel. *J. Environ. Radioact.* **2014**, *134*, 99−108.
(61) Attia, M. S.; Khalil, M. H.; Abdel-Mottaleb, M. S. A.; Lukyanova, M. B.; Alekseenko, Y. A.; Lukyanov, B. Effect of complexation with lanthanide metal ions on the photochromism of (1,3,3-trimethyl-s′-hydroxy-6′-formyl-indoline-spiro2,2′-[2h] chromene) in different media. *Int. J. Photoenergy* **2006**, *2006*, No. 042846.
(62) Attia, M. S.; Youssef, A. O.; Essawy, A. A. A novel method for tyrosine assessment in vitro by using fluorescence enhancement of the ion-pair tyrosine-neutral red dye photo probe. *Anal. Methods* **2012**, *4*, 2323−2328.
(63) Attia, M. S.; Diab, M.; El-Shahat, M. F. Diagnosis of some diseases related to the histidine level in human serum by using the nano optical sensor Eu−Norfloxacine complex. *Sens. Actuators, B* **2015**, *207*, 756−763.
(64) Elabd, A. A.; Attia, M. S. A new thin film optical sensor for assessment of UO22+ based on the fluorescence quenching of Trimetazidine doped in sol gel matrix. *J. Lumin.* **2015**, *165*, 179−184.
(65) Attia, M. S. Nano optical probe samarium tetracycline complex for early diagnosis of histidinemia in new born children. *Biosens. Bioelectron.* **2017**, *94*, 81−86.
(66) Essawy, A. A.; Attia, M. S. Novel application of pyronin y fluorophore as high sensitive optical sensor of glucose in human serum. *Talanta* **2013**, *107*, 18−24.
(67) Stern, O.; Völmer, M. Decay time of the fluorescence. *Z. Phys.* **1919**, *20*, 183−188.
(68) ICH Harmonised Tripartite Guideline. Validation of Analytical Procedures: Text and Methodology Q2(R1). In *International Conference on Harmonisation of Technical Requirements for Registration of Pharmaceuticals for Human Use*, European Medicines Agency: Geneva, 2005; pp 1−13.
(69) Kang, W. D.; Choi, H. S.; Kim, S. M. Value of serum CA125 levels in patients with high-risk, early stage epithelial ovarian cancer. *Gynecol. Oncol.* **2010**, *116*, 57−60.


https://doi.org/10.1021/acsomega.1c01974
*ACS Omega* 2021, 6, 20812−20821